Universality in quantum-critical flow of charge and heat in ultra-clean graphene

Aniket Majumdar,[1,*] Nisarg Chadha,[1,2] Pritam Pal,[1] Akash Gugnani,[1] Bhaskar Ghawri,[1] Kenji Watanabe,[3] Takashi Taniguchi,[4] Subroto Mukerjee,[1,†] and Arindam Ghosh[1,5,‡]

[1] *Department of Physics, Indian Institute of Science, Bangalore 560012, India*
[2] *Department of Physics, Harvard University, Cambridge, MA 02138, USA*
[3] *Research Center for Electronic and Optical Materials, National Institute for Materials Science, 1-1 Namiki, Tsukuba 305-0044, Japan*
[4] *Research Center for Materials Nanoarchitectonics, National Institute for Materials Science, 1-1 Namiki, Tsukuba 305-0044, Japan*
[5] *Center for Nano Science and Engineering, Indian Institute of Science, Bangalore 560012, India*

Close to the Dirac point, graphene is expected to exist in quantum critical Dirac fluid state, where the flow of both charge and heat can be described with a dc electrical conductivity σ_Q, and thermodynamic variables such as the entropy and enthalpy densities [1, 2]. Although the fluid-like viscous flow of charge is frequently reported in state-of-the-art graphene devices [3–15], the value of σ_Q, predicted to be quantized and determined only by the universality class of the critical point, has not been established experimentally so far [2, 16]. Here we have discerned the quantum critical universality in graphene transport by combining the electrical (σ) and thermal (κ_e) conductivities in very high-quality devices close to the Dirac point. We find that σ and κ_e are inversely related, as expected from relativistic hydrodynamics, and σ_Q converges to $\approx (4 \pm 1) \times e^2/h$ for multiple devices, where e and h are the electronic charge and the Planck's constant, respectively. We also observe, (1) a giant violation of the Wiedemann-Franz law where the Lorentz number exceeds the semiclassical value by more than 200 times close to the Dirac point at low temperatures, and (2) the effective dynamic viscosity (η_{th}) corresponds to $\eta_{th}/s_{th} \rightarrow \hbar/4\pi k_B$ within a factor of four, in the cleanest devices for $T_F/T \rightarrow 0$, where T_F, s_{th} and k_B are the Fermi temperature, thermal entropy density and the Boltzmann constant, respectively. Our experiment addresses the missing piece in the potential of high-quality graphene as a testing bed for some of the unifying concepts in physics.

Transport in real graphene devices is determined by two competing length scales: The electron-electron scattering length l_{ee} and the momentum relaxation length l_{mr}, both of which depend on the carrier density n (or the Fermi Temperature $T_F = \hbar v_F \sqrt{\pi n}/k_B$, v_F being the Fermi velocity) and the temperature T (see schematic in Fig. 1a). In the diffusive and inhomogeneous regimes, scattering from, for example, the Coulomb impurities or phonons, do not conserve the momentum, resulting in $l_{mr} \ll l_{ee}$. As the disorder decreases, the channel can be ballistic when the device dimension is $\ll l_{ee}$, l_{mr} or viscous, when l_{ee} becomes the shortest length scale. The viscous flow is described well by the electronic analogue of the Navier-Stokes equation [17] when $T_F/T \gg 1$, and manifests in parabolic propagation profile [5, 13], negative non-local resistance [4] or super-ballistic electrical conduction [7], among others.

In the opposite (thermal) limit of $T_F/T \ll 1$, nearly unscreened Coulomb interaction and linear dispersion tune to a Lorentz-invariant quantum critical point [2, 18], where the current relaxes by collisions among the thermally excited electrons and holes, while the energy propagates unimpeded due to conservation of momentum during such collisions. This naturally violates the Wiedemann-Franz (WF) law. For relativistic hydrodynamics, quantum critical σ and κ_e are predicted to be [19–21],

$$\sigma(n) = \sigma_Q + \frac{e^2 v_F n^2 l_{mr}}{\mathcal{H}} \tag{1}$$

and

$$\kappa_e(n) = \frac{v_F l_{mr} \mathcal{H} \sigma_Q}{T \sigma(n)} \tag{2}$$

where, $\mathcal{H}$ and v_F are the enthalpy density and Fermi velocity, respectively. So far, several experimental reports on the breakdown of the WF law [3], enhanced thermoelectric power [10], giant quasi-linear magnetoresistance [8], near-Planckian scattering rates and efficient thermal diffusion inferred from the terahertz [11] and pump-probe [9] spectroscopic techniques, provided valuable insight to the formation of a Dirac fluid, but unambiguous experimental evaluation of σ_Q has not been possible. This is because the measured σ for $n \rightarrow 0$ yields non-universal results, limited by device-dependent spatial inhomogeneity, or puddles, of charge close to the Dirac point [22] (see Supplementary Section S1). In the absence of this, the quantum critical behaviour itself remains unsettled, especially in the presence of alternative models that propose violation of the WF law in marginally gapped graphene within the Fermi liquid framework [23].

In this work, we have combined dc charge and heat transport to explore the quantum critical conductivity

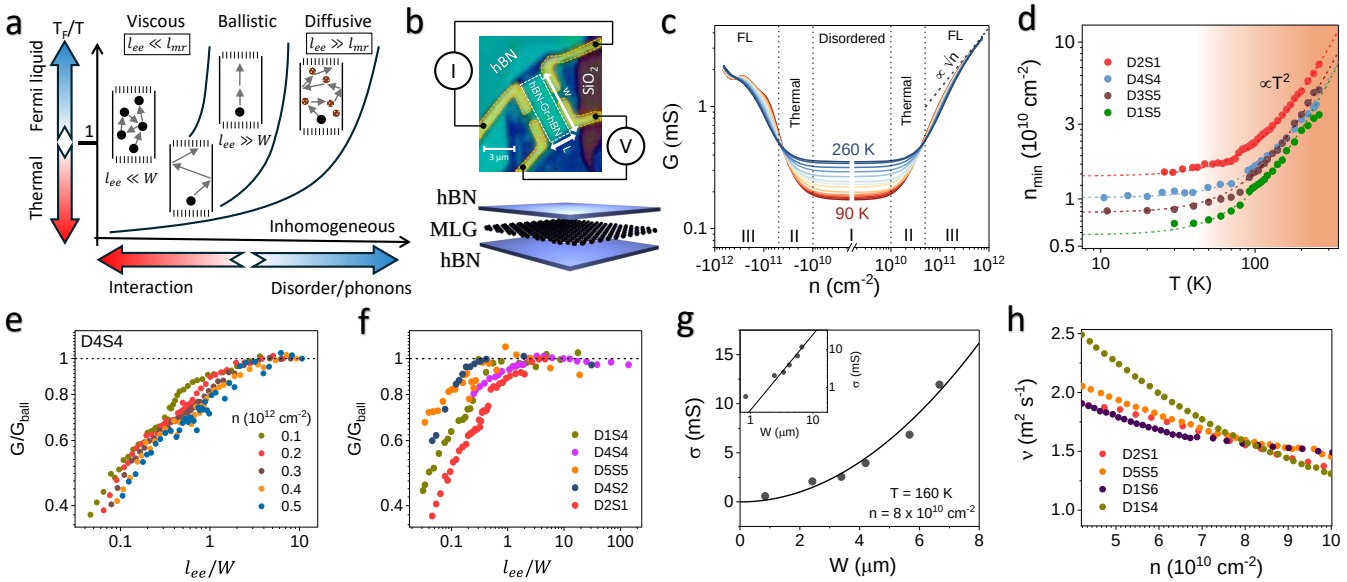

Figure 1: **Viscous electron flow in ultra-clean graphene devices:** (a) Different regimes of electron transport in graphene, based on the interplay between momentum-conserving and momentum-relaxing collisions. (b) (Top) Optical micrograph of the device along with the circuit diagram used for conducting the electrical transport measurements. (Bottom) Schematic of the heterostructure. (c) Electrical conductance of device D4S4 as a function of the carrier density n for 90 K $\leq T \leq$ 260 K. The dashed line labelled $G_{\rm ball}$ indicates the ballistic conductance for the measured channel. (d) Charge inhomogeneity ($n_{\rm min}$) as a function of T for five different devices. The colour gradient in the background indicates the transition from a disorder-driven regime to a thermally-driven transport regime. (e) Electrical conductance (normalised by the ballistic conductance, $G_{\rm ball}$) of D4S4 as a function of $l_{\rm ee}/W$ for different carrier densities, varying from $n = 1 \times 10^{11}$ cm^{-2} to 5×10^{11} cm^{-2}. (f) Normalised conductance as a function of the Knudsen number for five different devices. (g) Electrical conductivity as a function of width W at $n = 8 \times 10^{10}$ cm^{-2} and $T = 160$ K. For the chosen values of n and T, we have observed that $l_{\rm ee}/W \leq 0.5$. The solid line scales as W^2 and serves as a guide to the eye. Inset shows the same dataset in double logarithmic scale where the straight line represents quadratic dependence. (h) Kinematic viscosity ν as a function of n for four different devices, measured at $T = 180$ K.

in graphene. We measured both σ and $\kappa_{\rm e}$ in multiple graphene devices with low charge inhomogeneity $\simeq 5 - 10 \times 10^9$ cm^{-2}, where the momentum relaxation, particularly at low temperatures, occurs at the boundary in most of the devices [8]. Combining σ and $\kappa_{\rm e}$ as in Eqn. 2, and assigning $l_{\rm mr} = \min(W, l_{\rm mfp})$, where W and $l_{\rm mfp} = h\sigma/2e^2k_{\rm F}$ are the geometric channel width and the mean free path of carriers in the channel, respectively, we obtain a device-insensitive estimate of $\sigma_{\rm Q} \simeq (4\pm1)\times e^2/h$, where the error represents variation across multiple devices. Fundamentally, this *all-experimental* strategy to determine $\sigma_{\rm Q}$ depends on the high quality of our devices which makes the thermal limit ($T_{\rm F}/T < 1$) accessible over a broad range of T for $n \gtrsim n_{\rm min}(0)$, *i.e.*, when n is well-defined.

ELECTRON VISCOSITY IN THE ULTRA-CLEAN GRAPHENE DEVICES

All devices are single layers of graphene encapsulated with hexagonal boron nitride (hBN), which were etched into small rectangles of length L (≈ 1 to 2 μm) and width W, where W was varied between ≈ 1 to 8 μm (Figs. 1b, details in Methods, Table 1 and Supplementary Section S2). The variation of conductance (G) in a typical device (D4S4, see Table 1) with n for $T = 90 - 260$ K is shown in Fig. 1c. In the low-n limit, G becomes insensitive to n below a characteristic scale $n_{\rm min}(T)$, which increases with increasing T. The T-dependence of $n_{\rm min}(T)$, as shown for multiple devices in Fig. 1d, can be described with $n_{\rm min}(T) = n_{\rm min}(0) + \beta n_{\rm th}(T)$, where $n_{\rm min}(0)$ and $n_{\rm th}(T) = (2\pi^3/3)(k_{\rm B}T/hv_{\rm F})^2$ are the intrinsic inhomogeneity and the thermally excited carrier density, respectively (the prefactor β is $\approx 0.7 - 0.8$ for most devices, likely due to the residual charge inhomogeneity [24]). For the present experiments, we chose devices with $n_{\rm min}(0) \lesssim 10^{10}$ cm^{-2}, which usually exhibited lower Ra-

man linewidth and were occasionally subjected to post-fabrication current annealing (see Methods and Supplementary Section S2). The best devices exhibited carrier mobility as high as 5×10^5 cm^2/V.s and 6×10^6 cm^2/V.s at room temperature and low T ($\approx$ 10 K), respectively, for $n \approx 10^{11}$ cm^{-2} (see Supplementary Section S3 and Table I).

Fig. 1c identifies three distinct ranges in n. I: $n < n_{\rm min}(0)$, where the system is spatially inhomogeneous; II: the quasi-thermal regime, where $n_{\rm min}(0) < n \lesssim 8 \times 10^{10}$ cm^{-2}, for which $T_{\rm F}$ is lower than the maximum experimental T (300 K), and, III: $n \gtrsim 10^{11}$ cm^{-2}, where we expect the system to behave as Fermi liquid at all experimental T. In the large n ($\gtrsim 5 \times 10^{11}$ cm^{-2}) limit of regime III, the (four-terminal) conductance G approaches $\sim \sqrt{n}$ with a nearly T-independent magnitude $G_{\rm ball}$ (dashed line in Fig. 1c), that lies within a factor of about two of the Landauer-Sharvin conductance ($G_{\rm ls} = (4e^2/\pi h)k_{\rm F}W$). This is the ballistic regime where the Landauer-Sharvin conductance is delocalised into the bulk as a result of hydrodynamic flow that mediates the transfer of momentum among the propagating modes [12]. $G/G_{\rm ball}$ reduces from unity as n is decreased which may signify the onset of viscous flow (Fig. 1a). To examine this, we plot $G/G_{\rm ball}$ as a function of $l_{\rm ee}/W$ for a broad range of n in regime III of device D4S4 for which $l_{\rm mr} \approx W$ (Fig. 1e). We evaluated $l_{\rm ee} \approx \hbar v_{\rm F} T_{\rm F}/\alpha^2 k_{\rm B} T^2$ using the effective fine structure constant $\alpha \approx 0.5$ [25]. The onset of decrease in $G/G_{\rm ball}$ at $l_{\rm ee}/W \approx 1$ is evident in Fig. 1e. Since $l_{\rm ee}/W$ effectively represents the Knudsen number $\zeta (= l_{\rm ee}/l_{\rm mr})$ [6], this constitutes a strong evidence of the onset of Poiseuille flow. This behaviour was found to be generic in all high mobility devices, as shown for five different devices at $n = 10^{11}$ cm^{-2} in Fig. 1f, for which the momentum relaxation is expected to occur mainly at the boundaries (see Supplementary Section S3 for further details).

Strong Poiseuille-like flow of degenerate electrons requires the electronic Gurzhi length $D_\nu = \sqrt{\nu l_{\rm mr}/v_{\rm F}}$ to exceed W, where the conductivity $\sigma = GL/W = e^2 n^2 W^2/12\eta$ (Supplementary Sections S5 and S6) is then expected to vary quadratically with W [26] (here η, $\nu = \eta/\rho_{\rm m}$, and $\rho_{\rm m}$ are the dynamic viscosity, the kinematic viscosity, and the areal density of effective mass, respectively). In Fig. 1g, σ in multiple devices at fixed n ($\approx 8 \times 10^{10}$ cm^{-2}) and T (= 160 K), such that $T_{\rm F} \gtrsim T$ and $l_{\rm ee}/W < 1$ are simultaneously satisfied, is consistent with a quadratic dependence on W (see Fig. 1g inset). The quantitative estimate of ν, obtained from the n-dependence of σ at 180 K, is shown in Fig. 1h, where its magnitude $\sim 1.5 - 2$ m^2/s is nearly device-independent and agrees with previous reports [4, 7], as well as the theoretical calculations [27]. Since $l_{\rm mr}$ is limited by the boundaries in these devices, the observed ν confirms $D_\nu \gtrsim W$ and hence the strong Poiseuille-like flow. The differential resistance dV/dI also exhibits the characteristic non-monotonic dependence on the drive current density (Extended data Fig. 1), where the initial increase, followed by decrease, in dV/dI is attributed to crossover from the quasi-ballistic Knudsen flow to the Poiseuille regime.

THERMAL CONDUCTIVITY AND THE WIEDEMANN-FRANZ LAW

To examine the current and energy relaxation pathways, we have used Johnson noise thermometry [29] to determine the effective Lorentz number $\mathcal{L} = \kappa_{\rm e}/\sigma T$, and thereby the electronic thermal conductivity ($\kappa_{\rm e}$), at varying n and T. The experimental strategy, schematically shown in Fig. 2a (details in Supplementary Section S4), involves Joule heating the graphene layer with an external electric field E and evaluating the resulting increase in the electron temperature ($T_{\rm e}$) from the Johnson-Nyquist noise magnitude [3]. The weak coupling of electrons and phonons in graphene [30, 31] makes the Joule dissipation $P_{\rm J} = \sigma E^2$ rather effective to heat the electrons, leading to $T_{\rm e} \approx LE/\sqrt{\mathcal{L}}$ at large E, as shown for sample D2S1 for different n (at T = 30 K) and different T (at $n = 5 \times 10^{11}$ cm^{-2}) in Extended Data Fig. 2a and 2b, respectively. The dashed lines are fits according to Eqn. 6 (Methods) obtained from the spatially averaged solution for $T_{\rm e}$ from the heat diffusion equation with $\mathcal{L}$ as the (only) fit parameter. Evidently, $\mathcal{L}$ is strongly n and T-dependent, which underlines the breakdown of the WF law. The magnitude of $\mathcal{L}$ in the electron-doped part of D2S1 varies over six orders of magnitude as a function of n at low T (Fig. 2b, Extended Data Fig. 3), with a maximum value ($\mathcal{L}_0$) at the Dirac point that can exceed the universal magnitude $\mathcal{L}_{\rm WF} = (\pi^2/3)^2(k_{\rm B}/e)^2 = 2.44 \times 10^{-8}$ V^{2}K^{-2} from the WF law by nearly 300 times. Correspondingly, $\kappa_{\rm e} = \mathcal{L}\sigma T$ close to the Dirac point also exceeds the WF magnitude by similar order at low T. At large n however, *e.g.* at $n = 10^{11}$ cm^{-2}, $\kappa_{\rm e}$ is much lower than that expected from the WF law at all T, even though the electrical conductivity is significantly higher (Fig. 2b). The behaviour remains similar, albeit reduced, in lower mobility devices (D1S1, Extended Data Fig. 4) and indicates decoupling of the charge and heat flow expected in the hydrodynamic regime where $\mathcal{L}(n, T)$ varies as [21, 26],

$$\mathcal{L}(n,T) = \frac{1}{e^2}\left[\frac{s(T)n_0(T)}{n^2 + n_0^2(T)}\right]^2 \qquad (3)$$

Here, $n_0(T)$ is an effective density scale that determines the intrinsic conductivity of the electron fluid [26] (Extended data Fig. 5a). Semi-classical analysis considering small band gap opening at the Dirac point and various scattering mechanisms fail to explain the observed behaviour (Supplementary Section S7). Eqn. 3, however,

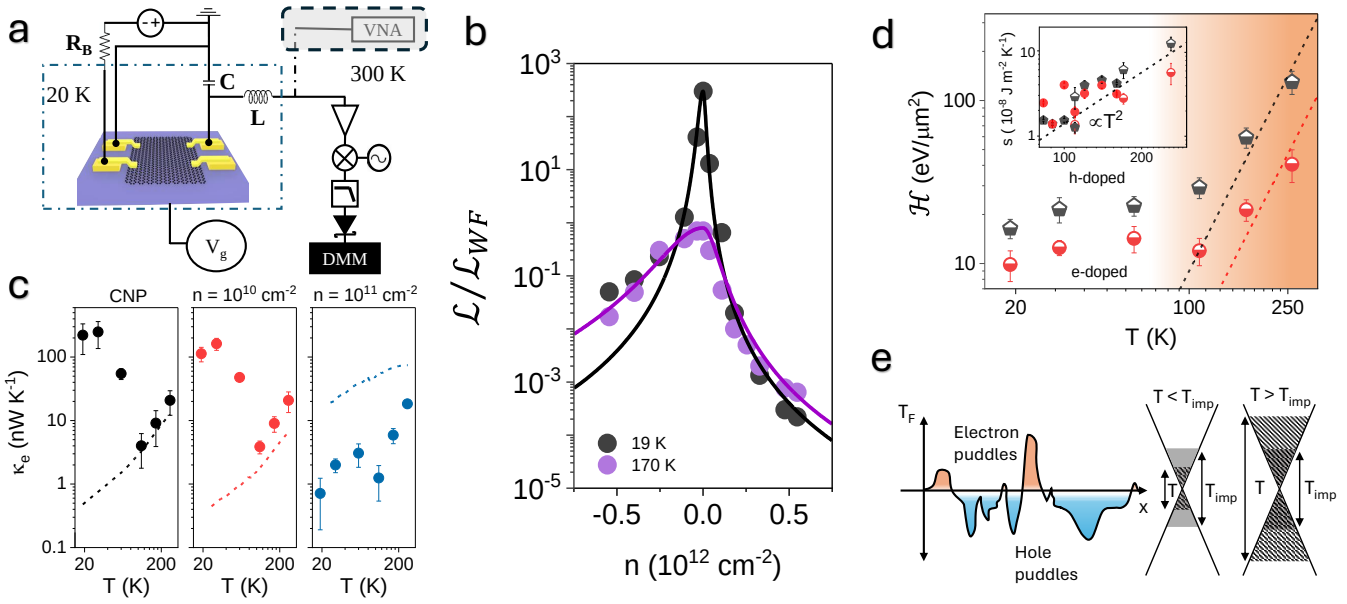

Figure 2: **Violation of the WF Law for hydrodynamic electrons:** (a) Circuit diagram for measuring Johnson-Nyquist noise of hot electrons in our graphene devices, when subjected to Joule heating by in-plane electric fields. The LC network acts as a tank circuit for impedance matching the graphene device to the 50 Ω noise measurement circuit. (b) Normalised Lorentz number for device D2S1 as a function of n for $T = 19$ K and 170 K. The solid lines are theoretical fits of the experimental data, as per Eqn. 3. The electron-doped and hole-doped data points have been fitted independently using different values for the fitting parameters. (c) Electronic component of thermal conductivity for device D2S1 as a function of T for 3 different number densities, from the charge neutrality point to a highly electron-doped regime. The dashed lines indicate the variation of thermal conductivity with T, assuming the normalised Lorentz number $\mathcal{L}/\mathcal{L}_{\rm WF} = 1$. (d) Enthalpy density ($\mathcal{H}$) for D2S1 as a function of T. The dashed lines (black - hole doped, red - electron doped) highlight T^3-like asymptotic behaviour. The colour gradient in the background signifies a transition from a disorder-driven regime to a thermally-driven transport regime. [Inset] Entropy density for D2S1 as a function of T for $T > 80$ K. The black dashed line is the T^2 fit of the experimentally obtained data and is within a factor of 2 of what is expected from the theoretical expression in Ref. [28]. (e) Schematic showing the interplay between two different types of electrical transport - disorder-driven and thermal excitation-driven. For $T < T_{\rm imp}$, the energy scale of the background potential fluctuations is greater than the thermal energy of electrons and hence the electrical transport is dominated by charged impurities and defects, whereas for $T > T_{\rm imp}$, the electronic thermal energy dominates and electron-electron interactions drive electrical transport in this regime.

fits very well (solid lines in Fig. 2c) to the experimentally observed dependence of $\mathcal{L}$ on n, especially in the electron doped regime. These fits also provide experimental estimation of two key thermodynamic variables associated with the hydrodynamic flow, namely the entropy $s(T) = en_0\sqrt{\mathcal{L}_0}$ and, from Gibb's equation, the enthalpy $\mathcal{H}(T) = Ts(T)$ densities. The dependence of $\mathcal{H}$ and s on T are shown in Fig. 2d and its inset, respectively.

An important temperature scale, identified by the non-monotonic behaviour of $\mathcal{L}_0$ (Extended data Fig. 5b), is $T \sim T_{\rm imp} = \hbar v_{\rm F}\sqrt{\pi n_{\rm min}(0)}/2k_{\rm B} \approx 80$ K, determined by the fluctuations in local chemical potential from intrinsic disorder. For $T \ll T_{\rm imp}$, the incompressibility of graphene arrests the fluctuations in n to $\sim n_{\rm min}(0)$, which saturates $\mathcal{H}$ to the T-independent Fermi liquid contribution ($\mathcal{H}_0$). The thermal component $\mathcal{H}_{\rm th} \sim T^3$ dominates only for $T \gtrsim T_{\rm imp}$ (dashed lines in Fig. 2d). The scenario is schematically explained in Fig. 2e. For D2S1, we find $\mathcal{H}_0 \sim \rho_{\rm m0}v_{\rm F}^2 = 3.5$ eV/μm^2 within a factor of ~ 3 of the observed enthalpy at low temperatures (here, $\rho_{\rm m0}$ is the mass density at $n_{\rm min}(0)$). Moreover, an estimate of $\mathcal{L}_0 \approx v_{\rm F}W\mathcal{H}_0/\sigma_{\rm min}T^2$ at $T \ll T_{\rm imp}$ from Eqn. 2 suggests $\mathcal{L}_0/\mathcal{L}_{\rm WF} \approx 500$ at $T = 20$ K, which is within a factor of two of that observed experimentally.

QUANTUM CRITICAL TRANSPORT IN THE THERMAL REGIME

Having established the dominance of the electron-electron scattering rate over that of momentum relaxation in our devices, we now focus on the thermal regime

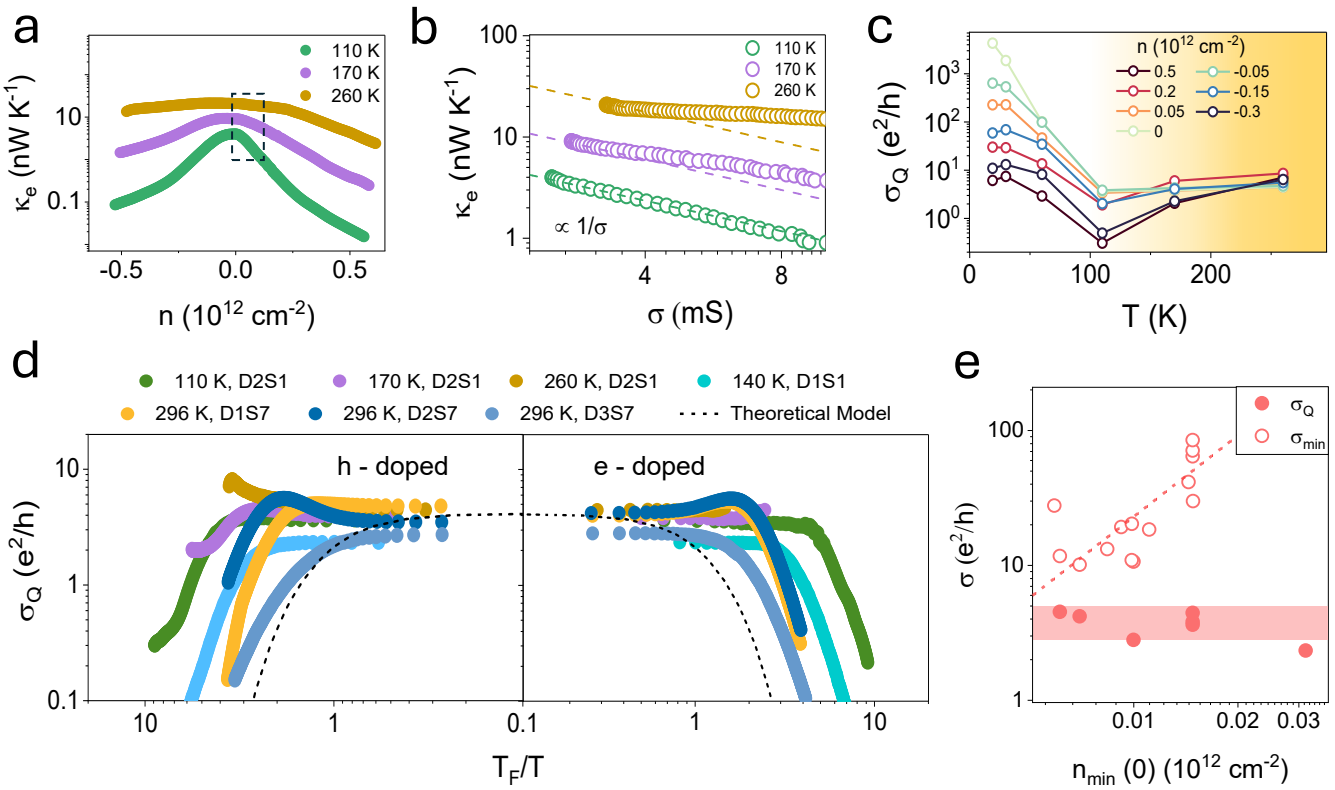

Figure 3: **Universality of the quantum critical conductivity:** (a) Electronic component of thermal conductivity (κ_e) for device D2S1 as a function of n for $T = 110$ K, 170 K and 260 K. (b) κ_e as a function of electrical conductivity σ for device D2S1 at three different temperatures from the region indicated by the bounding box in panel (a). The dashed lines indicate a $1/\sigma$ dependence and serve as a guide to the eye. (c) σ_Q for D2S1 as a function of T for a range of densities from $n = -3 \times 10^{11}$ cm^{-2} (hole-doped) to $n = 5 \times 10^{11}$ cm^{-2} (electron-doped). The shaded region corresponds to temperatures greater than the scale of background chemical potential fluctuations. (d) σ_Q as a function of the ratio of Fermi temperature to absolute temperature (T_F/T), calculated at different temperatures for four different devices. The dashed line is based on theoretical calculations performed in Ref. [25]. (e) Comparison of the quantum critical conductivity σ_Q (obtained from thermal transport measurements) and the minimum electrical conductivity σ_{min} (obtained from electrical transport measurements at $T < 60$ K), as a function of the intrinsic charge inhomogeneity $n_{min}(0)$. The dashed line scales as $n^2_{min}(0)$ and serves as a guide to the eye.

where we expect the system to behave as a quantum-critical Dirac fluid. The rapid increase in $\mathcal{H}(T)$ at $T \gtrsim T_{imp}$ (Fig. 2d) suggests the onset of the thermal regime, where the corresponding entropy density $s_{th}(T) = s(T \gtrsim 100\text{ K}) = \mathcal{H}/T$ is $\propto T^2$ (inset of Fig. 2d). The observed magnitude of $s_{th}(T) = cs_{theory}(T)$ agrees closely with the theoretically predicted entropy density $s_{theory}(T)$ [28], where the numerical constant c lies between 0.5 and 2 for all devices measured. Subsequently, multiplying σ to the fitted expression of $\mathcal{L}(n)$ yields n-dependence of κ_e as shown for three values of $T > T_{imp}$ in Fig. 3a. Obtaining κ_e and σ for the same n ($\lesssim 10^{11}$ cm^{-2}), we find κ_e to *decrease* with *increasing* σ (Fig. 3b), which cannot be explained within a Fermi liquid framework, and points towards the relativistic hydrodynamic description described by Eqn. 2.

Combining κ_e, σ and s_{th}, each of which is obtained from either directly or through analysis of the transport and noise measurements, we then compute $\sigma_Q = \kappa_e\sigma/v_F l_{mr} s_{th}$ (Details in Supplementary Section S8), and first show it as a function of T for different n in Fig. 3c. Beyond the inhomogeneous puddle-dominated regime (*i.e.* $T \lesssim 80$ K) (shaded region in Fig. 3c), it is evident that close to the charge neutrality point ($|n| \lesssim 5 \times 10^{10}$ cm^{-2}), σ_Q approaches $\approx 4e^2/h$, and is nearly independent of temperature. For larger n ($\gtrsim 5 \times 10^{10}$ cm^{-2}), σ_Q is lower than this value in both the electron and the hole-doped regimes. This is further emphasized when σ_Q is plotted against T_F/T for different devices and temperatures ($\gtrsim T_{imp}$), where it follows very similar trajectories that converge to $(4 \pm 1) \times e^2/h$ for $T_F/T \ll 1$, and drops sharply for $T_F/T \gg 1$ (Fig. 3d).

To distinguish between $\sigma_{\rm min}$ and $\sigma_{\rm Q}$, we have compared these two parameters for all devices in Fig. 3e. $\sigma_{\rm min}$ is clearly non-universal and increases rapidly with disorder ($n_{\rm min}(0)$) by more than an order with the dashed line suggesting $\sim n^2_{\rm min}(0)$ dependence, whereas $\sigma_{\rm Q}$ varies by $\lesssim 25\%$ (shaded region).

The device independence of $\sigma_{\rm Q}$ can be readily attributed to the universality of dc conductivity of hydrodynamic transport in the presence of incoherent electron-hole collisions, for example, that at superfluid-insulator transition [16, 32]. This quantum critical conductivity is predicted to be quantized to $4e^2\Phi/h$, where $\Phi \sim \mathcal{O}[1]$ is a dimensionless number dependent only on the universality class of the critical point [2, 16]. The observed convergence of $\sigma_{\rm Q}$ to $\sim 4e^2/h$ in Fig. 3d for $T_{\rm F}/T \ll 1$ is consistent with this scenario. As $|n|$ increases away from the Dirac point, $\sigma_{\rm Q}$ scales as $\sim (4e^2/h)f(T/T_{\rm F})$, where f is a function of the dimensionless parameter $T_{\rm F}/T$. For $T_{\rm F}/T \gtrsim 1$, f decreases rapidly, which is because of the suppression of the relativistic physics and quantum criticality as the system crosses over from the zero to the finite-momentum mode [25].

DISCUSSION

With the temperature as the only energy scale left, we will now estimate the effective viscosity $\eta_{\rm th} = \mathcal{H}_{\rm th}\tau_{\rm P}/2$ in the thermal regime, where we assume the current relaxation to occur by electron-hole collisions at the Planckian rate $\tau_{\rm P}^{-1} \approx \alpha^2 k_{\rm B}T/\hbar$ [11]. Notably, no such assumption was required in the evaluation of the quantum-critical conductivity $\sigma_{\rm Q}$. The hydrodynamicity of charge flow is then expected to result in a quadratic n-dependence of σ (Eqn. 1), which we can indeed identify in our high-quality devices between $|n| \gtrsim n_{\rm min}(0) \sim 10^{10}$ cm^{-2}, and $T_{\rm F} \lesssim T$, as shown for D2S1 in the inset of Fig. 4a (see Extended Data Fig. 6 for other devices). This allows us to estimate $\eta_{\rm th} = e^2 v_{\rm F} W \tau_{\rm P}/2A_{\rm th}(T)$, where $A_{\rm th}(T)$ is the coefficient of n^2 in the n-dependence of σ.

$\eta_{\rm th}$ varies nonmonotonically with a minimum around $T \sim T_{\rm imp}$. For $T \gtrsim T_{\rm imp}$, $\eta_{\rm th}$ increases and approaches $\sim T^2$ dependence at high T [28] (Fig. 4a, details in Supplementary Section S9). Finally, with $\eta_{\rm th}$ estimated from the σ as above and $s_{\rm th}$ obtained from thermal conductivity (dashed line in Fig. 2d, inset), we have computed the ratio $\eta_{\rm th}/s_{\rm th}$ normalized by its universal limit $\hbar/4\pi k_{\rm B}$ [33]. Within the holographic description, the normalised $\eta_{\rm th}/s_{\rm th}$ is expected to approach unity for minimally dissipative flow of strongly interacting quantum liquids, limited only by the Heisenberg's uncertainty principle [34]. We have plotted the normalised $\eta_{\rm th}/s_{\rm th}$ as a function of T for both electron and hole-doped regimes for several devices in Fig. 4b. At $T < T_{\rm imp} \sim 100$ K, the variation in $\eta_{\rm th}/s_{\rm th} \sim 1/T^3$, represented by the open symbols and solid lines in the left inset of Fig. 4b, is consistent with

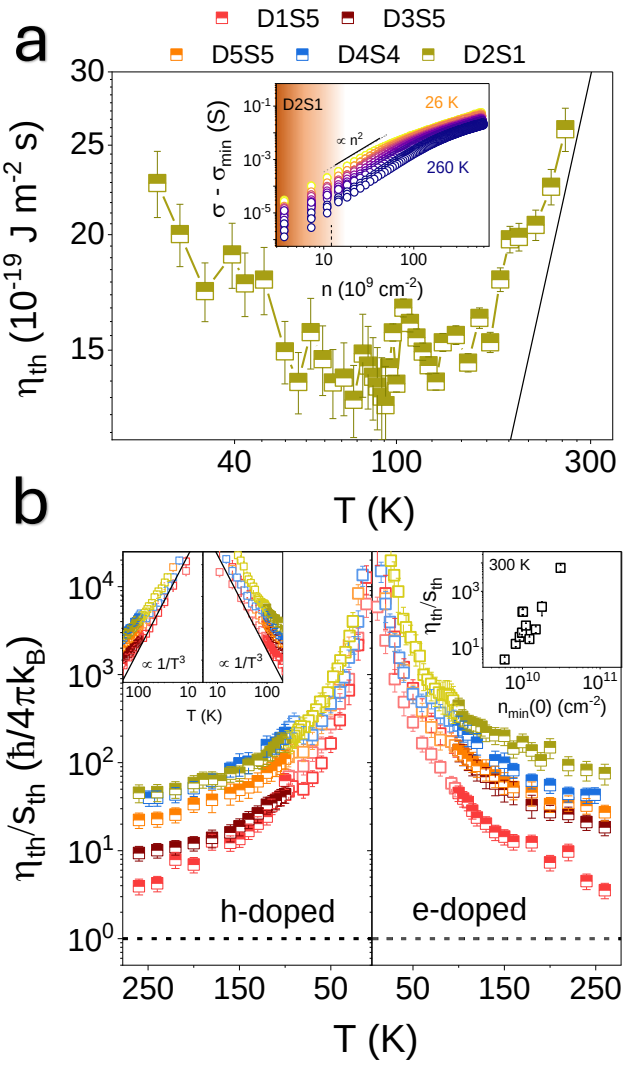

Figure 4: **Thermal viscosity in ultra-clean graphene:** (a) Thermal shear viscosity ($\eta_{\rm th}$) for D2S1 as a function of T. The solid line indicates an asymptotic T^2 dependence. [Inset] The quadratic density dependence of $\sigma - \sigma_{\rm min}$ where the inhomogeneity regime ($n < n_{\rm min}(0) \approx 10^{10}$ cm^{-2}) is indicated through shading. The upper limit of this range is marked by a dashed line, which represents $n_{\rm min}(0)$.(b) $\eta_{\rm th}/s_{\rm th}$ as a function of T for both the electron- and hole-doped regimes, in five different devices. The dashed line indicates the holographic lower bound. The data for $T < T_{\rm imp}$ have been indicated using open symbols. [Left inset] $\eta_{\rm th}/s_{\rm th}$ in double logarithmic scale to indicate the power law dependence on temperature (solid lines). [Right inset] Dependence of $\eta_{\rm th}/s_{\rm th}$ on $n_{\rm min}(0)$ at $T = 300$ K.

that expected from a degenerate Fermi liquid [33], where the chemical potential close to the Dirac point is pinned to the inhomogeneity scale (Fig. 2e). For $T \gg T_{\rm imp}$, however, $\eta_{\rm th}/s_{\rm th}$ tends to saturate, but the saturation occurs

to lower values when the channel disorder is decreased, and for the cleanest channel D1S5 (see Table 1), $\eta_{\rm th}/s_{\rm th}$ approaches $\hbar/4\pi k_{\rm B}$ within a factor of 4. The sensitivity of the limiting $\eta_{\rm th}/s_{\rm th}$ to disorder, quantified by $n_{\rm min}(0)$, in Fig. 4b (right inset), is quite striking, and could be due to increase in the shear viscosity in the presence of disorder scattering in Dirac fluids [35].

In conclusion, we report signatures of viscous electron flow and quantum critical transport in extremely clean monolayer graphene devices with charge inhomogeneity scale as low as $\sim 5 \times 10^9$ cm^{-2}. At the charge neutrality point, we find the electronic thermal conductivity to exceed that expected from the WF law by nearly 300 times at low temperatures. Combining electrical and thermal transport measurements, we could evaluate the intrinsic dc quantum critical conductivity $\sigma_{\rm Q} \approx 4e^2/h$, with device-to-device variation $\lesssim \pm 25\%$. Considering a Planckian scattering-limited electronic viscosity, we also demonstrate that the ratio of viscosity to thermal entropy density $\rightarrow \hbar/4\pi k_{\rm B}$, the holographic limit, within about a factor of four in the cleanest devices at room temperature. Apart from unifying some of the deep conceptual frameworks in physics, our results will impact the analysis and interpretation of both dc charge and heat transport in monolayer graphene, as the quality of such devices continues to improve.

METHODS

Fabrication of hBN-encapsulated graphene heterostructures

All the devices presented in this work have been assembled using a manually operated transfer setup. The graphene (Gr) and hexagonal boron nitride (hBN) flakes were mechanically exfoliated from bulk graphite (obtained from KishGraphite) and bulk hBN crystals (obtained from NIMS, Japan) respectively, using a combination of both scotch-tape and hot exfoliation. Subsequently, the thickness of the flakes was confirmed using atomic force microscopy (AFM) and Raman spectroscopy. Further, the cleanliness of the individual flakes was qualitatively characterised using the surface roughness of flakes obtained from AFM line scans and the peak line widths obtained from Raman spectroscopy (Supplementary Section S2). These flakes were thereafter stacked into a van der Waals (vdW) heterostructure on a Si/SiO_2 substrate using a dry-transfer technique that involves coating a PPC (Polypropylene Carbonate) film on a hemispherical PDMS (Polydimethylsiloxane) drop. The transferred vdW heterostructure was etched into a rectangular shape using e-beam lithography, followed by reactive ion etching using a mixture of O_2 and CHF_3 gases. Finally, electrical contacts were deposited on the heterostructure via thermal evaporation of Cr (5 nm) and Au (60 nm).

Transport measurements

The electrical and thermal transport characterisation of the devices was carried out in a home-made He-4 Cryostat and in the s200 4K Cryostation (Montana Instruments), respectively. The temperature-dependent transfer characteristics were measured using a SR830 Lock-in Amplifier and a Keithley 2400 Source Meter. The differential conductance measurements were carried out using an AC-DC mixer circuit, where the AC signal was sourced and measured using a Lock-in Amplifier, while the DC signal was sourced from a Keithley 2400 Source Meter and measured using a Keithley 2182A Nanovoltmeter. The thermal transport measurements were carried out using a high-frequency compatible Johnson noise thermometry setup, whose schematic has been detailed in Supplementary Section S4.

Solution of the heat diffusion equation

The DC electric field applied across the contacts of the device leads to the formation of a thermal gradient across the device. The spatial distribution of the thermal gradient is ideally governed by the heat diffusion equation. However, under experimental conditions, it can be reduced to the 1D Fourier's equation, which is given by

$$q = -\kappa_{\rm e} \nabla T_{\rm e}(x) \tag{4}$$

where q is the rate of heat flow into the channel and $T_{\rm e}(x)$ is the electron temperature at any point x along the direction of current flow.

For our graphene device, the rate of power influx is equal to the power dissipated at the contacts.

$$q = JWEL \tag{5}$$

where W and L are, respectively, the width and length of the channel.

If we assume the thermal gradient to primarily be in the direction of the applied electric field, the above equation can be solved to get the following solution:

$$T_{\rm e}(x) = \begin{cases} \sqrt{T_{\rm c}^2 + \dfrac{2L}{\mathcal{L}} E^2 x} & \text{for } 0 \le x \le L/2 \\ \sqrt{T_{\rm c}^2 + \dfrac{2L}{\mathcal{L}} E^2 (L-x)} & \text{for } L/2 \le x \le L \end{cases}$$

where $T_{\rm c}$ is the temperature of the metallic electrode.

The measured thermal noise gives us an average electron temperature ($T_{\rm e}$), integrated over the entire surface area of the device and it is given by

$$T_{\rm e} = \frac{2\mathcal{L}}{3L^2E^2} \left[\left(T_{\rm c}^2 + \frac{L^2}{\mathcal{L}} E^2 \right)^{3/2} - \left(T_{\rm c}^2 \right)^{3/2} \right] \tag{6}$$

Detailed derivation of this calculation has been presented in Supplementary Section S10.

DATA AVAILABILITY

All data files are available from the corresponding author upon request.

CODE AVAILABILITY

The code used for theoretical simulations present in the Supplementary Information is available in the linked Github repository.

ACKNOWLEDGMENT

The authors gratefully acknowledge the usage of the MNCF and NNFC facilities at CeNSE, IISc. The authors would also like to acknowledge fruitful discussions with D. Sen, A. Lucas, S. Sachdev, A. Hui, B. Skinner, N. Trivedi, M. Randeria, B. Dora, R. Moessner, A. Green and S. Sondhi. A.G. acknowledges financial support from a project under NanoMission, Department of Science and Technology, India and J. C. Bose Fellowship. P.P. and Ak.G. thank the Ministry of Education, Govt. of India for the Prime Minister's Research Fellowship (PMRF). K.W. and T.T. acknowledge support from the JSPS KAKENHI (Grant Numbers 21H05233 and 23H02052) and World Premier International Research Center Initiative (WPI), MEXT, Japan.

ETHICS DECLARATION

The authors declare no competing interests.

* aniketm@iisc.ac.in
† smukerjee@iisc.ac.in
‡ arindam@iisc.ac.in

[1] D. Son, Quantum critical point in graphene approached in the limit of infinitely strong coulomb interaction, Phys. Rev. B - Cond. Mat. and Mat. Phys. **75**, 235423 (2007).
[2] S. A. Hartnoll, P. K. Kovtun, M. Müller, and S. Sachdev, Theory of the Nernst effect near quantum phase transitions in condensed matter and in dyonic black holes, Phys. Rev. B **76**, 144502 (2007).
[3] J. Crossno, J. K. Shi, K. Wang, X. Liu, A. Harzheim, A. Lucas, S. Sachdev, P. Kim, T. Taniguchi, K. Watanabe, *et al.*, Observation of the Dirac fluid and the breakdown of the Wiedemann-Franz law in graphene, Science **351**, 1058 (2016).
[4] D. Bandurin, I. Torre, R. K. Kumar, M. Ben Shalom, A. Tomadin, A. Principi, G. Auton, E. Khestanova, K. Novoselov, I. Grigorieva, *et al.*, Negative local resistance caused by viscous electron backflow in graphene, Science **351**, 1055 (2016).
[5] M. J. Ku, T. X. Zhou, Q. Li, Y. J. Shin, J. K. Shi, C. Burch, L. E. Anderson, A. T. Pierce, Y. Xie, A. Hamo, *et al.*, Imaging viscous flow of the Dirac fluid in graphene, Nature **583**, 537 (2020).
[6] D. A. Bandurin, A. V. Shytov, L. S. Levitov, R. K. Kumar, A. I. Berdyugin, M. Ben Shalom, I. V. Grigorieva, A. K. Geim, and G. Falkovich, Fluidity onset in graphene, Nat. Commun. **9**, 4533 (2018).
[7] R. Krishna Kumar, D. Bandurin, F. Pellegrino, Y. Cao, A. Principi, H. Guo, G. Auton, M. Ben Shalom, L. A. Ponomarenko, G. Falkovich, *et al.*, Superballistic flow of viscous electron fluid through graphene constrictions, Nat. Phys. **13**, 1182 (2017).
[8] N. Xin, J. Lourembam, P. Kumaravadivel, A. Kazantsev, Z. Wu, C. Mullan, J. Barrier, A. A. Geim, I. Grigorieva, A. Mishchenko, *et al.*, Giant magnetoresistance of Dirac plasma in high-mobility graphene, Nature **616**, 270 (2023).
[9] A. Block, A. Principi, N. C. Hesp, A. W. Cummings, M. Liebel, K. Watanabe, T. Taniguchi, S. Roche, F. H. Koppens, N. F. van Hulst, *et al.*, Observation of giant and tunable thermal diffusivity of a Dirac fluid at room temperature, Nat. Nanotechnol. **16**, 1195 (2021).
[10] F. Ghahari, H. Y. Xie, T. Taniguchi, K. Watanabe, M. S. Foster, and P. Kim, Enhanced thermoelectric power in graphene: Violation of the Mott relation by inelastic scattering, Phys. Rev. Lett. **116**, 136802 (2016).
[11] P. Gallagher, C.-S. Yang, T. Lyu, F. Tian, R. Kou, H. Zhang, K. Watanabe, T. Taniguchi, and F. Wang, Quantum-critical conductivity of the Dirac fluid in graphene, Science **364**, 158 (2019).
[12] C. Kumar, J. Birkbeck, J. A. Sulpizio, D. Perello, T. Taniguchi, K. Watanabe, O. Reuven, T. Scaffidi, A. Stern, A. K. Geim, *et al.*, Imaging hydrodynamic electrons flowing without Landauer–Sharvin resistance, Nature **609**, 276 (2022).
[13] J. A. Sulpizio, L. Ella, A. Rozen, J. Birkbeck, D. J. Perello, D. Dutta, M. Ben-Shalom, T. Taniguchi, K. Watanabe, T. Holder, *et al.*, Visualizing Poiseuille flow of hydrodynamic electrons, Nature **576**, 75 (2019).
[14] W. Huang, T. Paul, K. Watanabe, T. Taniguchi, M. L. Perrin, and M. Calame, Electronic Poiseuille flow in hexagonal boron nitride encapsulated graphene field effect transistors, Phys. Rev. Res. **5**, 023075 (2023).
[15] C. Tan, D. Y. Ho, L. Wang, J. I. Li, I. Yudhistira, D. A. Rhodes, T. Taniguchi, K. Watanabe, K. Shepard, P. L. McEuen, *et al.*, Dissipation-enabled hydrodynamic conductivity in a tunable bandgap semiconductor, Sci. Adv. **8**, eabi8481 (2022).
[16] K. Damle and S. Sachdev, Nonzero-temperature transport near quantum critical points, Phys. Rev. B **56**, 8714 (1997).
[17] L. Levitov and G. Falkovich, Electron viscosity, current vortices and negative nonlocal resistance in graphene, Nat. Phys. **12**, 672 (2016).
[18] L. Fritz, J. Schmalian, M. Müller, and S. Sachdev, Quantum critical transport in clean graphene, Phys. Rev. B **78**, 085416 (2008).

[19] A. Lucas, J. Crossno, K. C. Fong, P. Kim, and S. Sachdev, Transport in inhomogeneous quantum critical fluids and in the Dirac fluid in graphene, Phys. Rev. B **93**, 075426 (2016).

[20] H. Y. Xie and M. S. Foster, Transport coefficients of graphene: Interplay of impurity scattering, Coulomb interaction, and optical phonons, Phys. Rev. B **93**, 195103 (2016).

[21] A. Lucas and K. C. Fong, Hydrodynamics of electrons in graphene, J. Phys. : Cond. Mat. **30**, 053001 (2018).

[22] S. Adam, E. Hwang, V. Galitski, and S. Das Sarma, A self-consistent theory for graphene transport, PNAS **104**, 18392 (2007).

[23] Y.-T. Tu and S. D. Sarma, Wiedemann-Franz law in graphene, Phys. Rev. B **107**, 085401 (2023).

[24] L. A. Ponomarenko, A. Principi, A. D. Niblett, W. Wang, R. V. Gorbachev, P. Kumaravadivel, A. I. Berdyugin, A. V. Ermakov, S. Slizovskiy, K. Watanabe, *et al.*, Extreme electron–hole drag and negative mobility in the Dirac plasma of graphene, Nat. Commun. **15**, 9869 (024).

[25] M. Müller, L. Fritz, and S. Sachdev, Quantum-critical relativistic magnetotransport in graphene, Phys. Rev. B - Cond. Mat. and Mat. Phys. **78**, 115406 (2008).

[26] S. Li, A. Andreev, and A. Levchenko, Hydrodynamic electron transport in graphene Hall-bar devices, Phys. Rev. B **105**, 155307 (2022).

[27] F. M. Pellegrino, I. Torre, A. K. Geim, and M. Polini, Electron hydrodynamics dilemma: Whirlpools or no whirlpools, Phys. Rev. B **94**, 155414 (2016).

[28] I. Yudhistira, R. Afrose, and S. Adam, Non-monotonic temperature dependence of electron viscosity and crossover to high-temperature universal viscous fluid in monolayer and bilayer graphene, arXiv preprint arXiv:2312.09701 (2023).

[29] A. C. Betz, F. Vialla, D. Brunel, C. Voisin, M. Picher, A. Cavanna, A. Madouri, G. Fève, J.-M. Berroir, B. Plaçais, and E. Pallecchi, Hot electron cooling by acoustic phonons in graphene, Phys. Rev. Lett. **109**, 056805 (2012).

[30] A. C. Ferrari, J. C. Meyer, V. Scardaci, C. Casiraghi, M. Lazzeri, F. Mauri, S. Piscanec, D. Jiang, K. S. Novoselov, S. Roth, *et al.*, Raman spectrum of graphene and graphene layers, Phys. Rev. Lett. **97**, 187401 (2006).

[31] K. C. Fong, E. E. Wollman, H. Ravi, W. Chen, A. A. Clerk, M. Shaw, H. Leduc, and K. Schwab, Measurement of the Electronic Thermal Conductance Channels and Heat Capacity of Graphene at Low Temperature, Phys. Rev. X **3**, 041008 (2013).

[32] M. P. Fisher, G. Grinstein, and S. Girvin, Presence of quantum diffusion in two dimensions: Universal resistance at the superconductor-insulator transition, Phys. Rev. Lett. **64**, 587 (1990).

[33] M. Müller, J. Schmalian, and L. Fritz, Graphene: A nearly perfect fluid, Phys. Rev. Lett. **103**, 025301 (2009).

[34] P. K. Kovtun, D. T. Son, and A. O. Starinets, Viscosity in strongly interacting quantum field theories from black hole physics, Phys. Rev. Lett. **94**, 111601 (2005).

[35] W. Chen and W. Zhu, Viscosity of disordered Dirac electrons, Phys. Rev. B **106**, 014205 (2022).

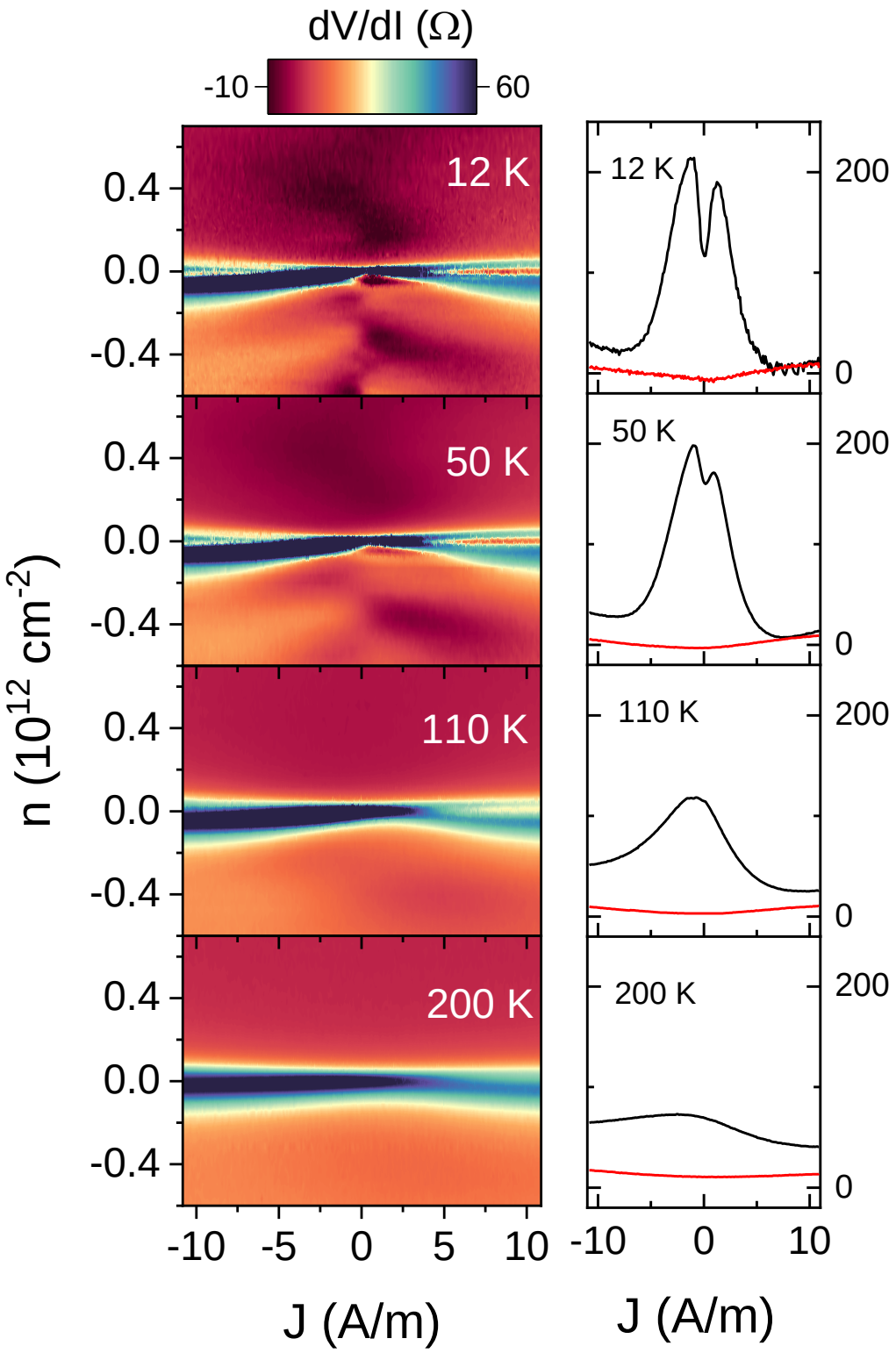

Extended Data Figure 1: **Differential resistance measurements showing crossover from Knudsen to Poiseuille regime:** (Left side) Colour plot showing the variation of dV/dI for D3S5 as a function of n and applied electrical current density (J) at four different T. (Right side) Line plots, obtained from the respective colour plots on the left, depicting the variation of dV/dI as a function of applied electrical current density (J) for two distinct number densities: $n = 10^{10}$ cm^{-2} (marked in black) and $n = 10^{11}$ cm^{-2} (marked in red).

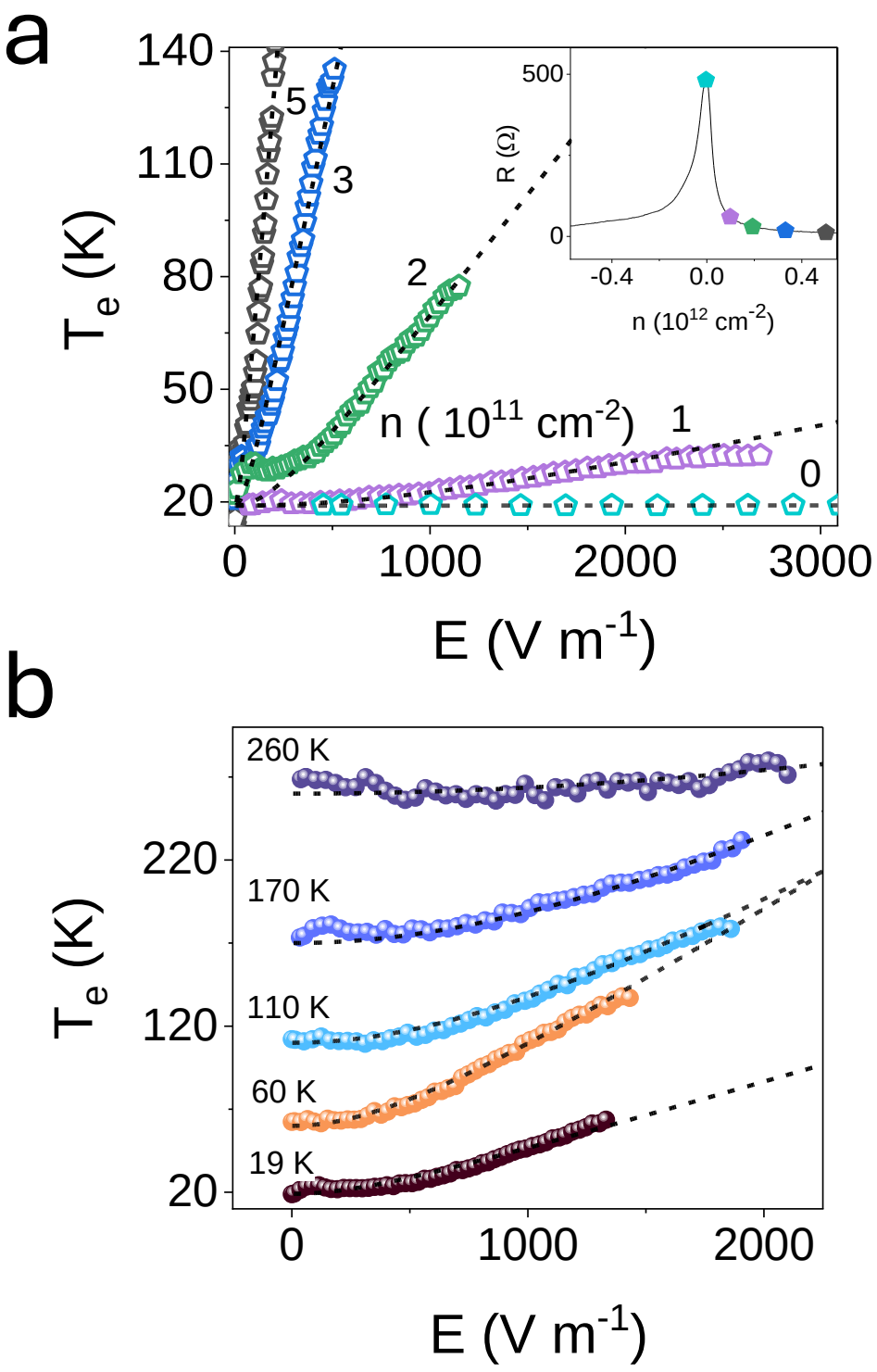

Extended Data Figure 2: **Electronic temperature across the graphene channel at low electric fields:** (a) T_e in D2S1 as a function of the applied electric field (E) at different electron densities, recorded at $T = 19$ K. The dashed lines are theoretically fitted curves for the experimental data, following Eqn. 6. [Inset] Transfer characteristics of the device D2S1 at 19 K, with colored dots indicating the resistance at the different n at which T_e vs E data has been recorded. (b) T_e as a function of the applied electric field (E) at different temperatures, for $n = 5 \times 10^{11}$ cm^{-2}.

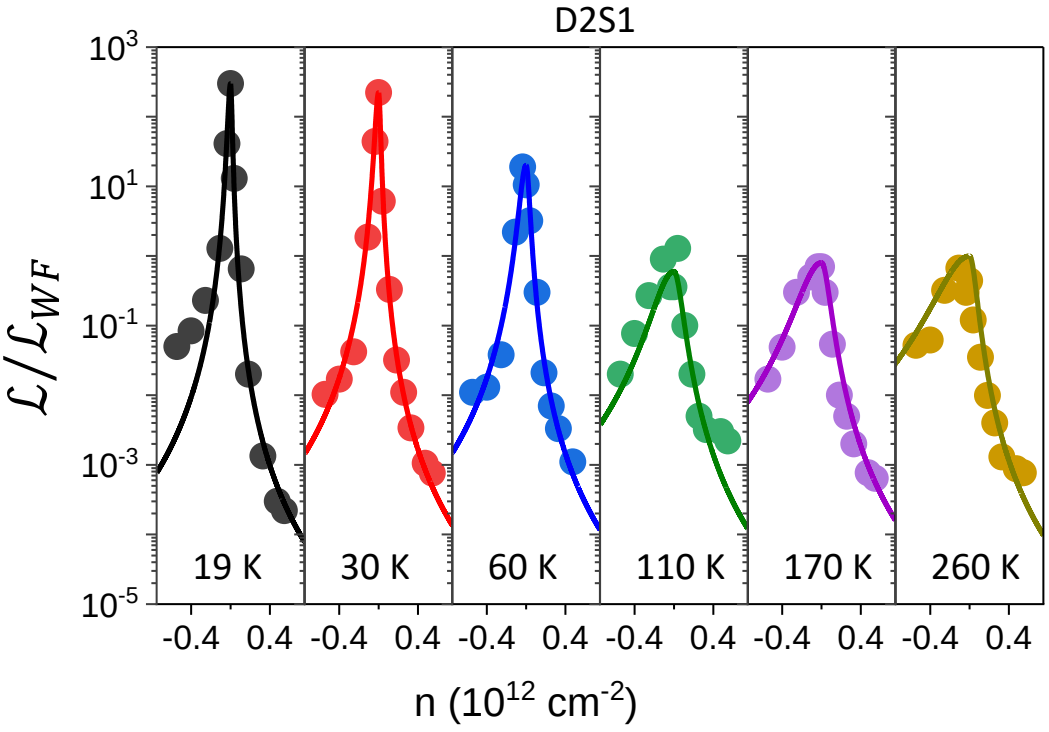

Extended Data Figure 3: **Violation of WF Law in D2S1 at six different temperatures:** Normalised Lorentz ratio ($\mathcal{L}/\mathcal{L}_{WF}$) for D2S1, as a function of n for $T = 19$ K, 30 K, 60 K, 110 K, 170 K and 260 K. The solid lines are theoretical fits for the experimental data, as per Eqn. 3.

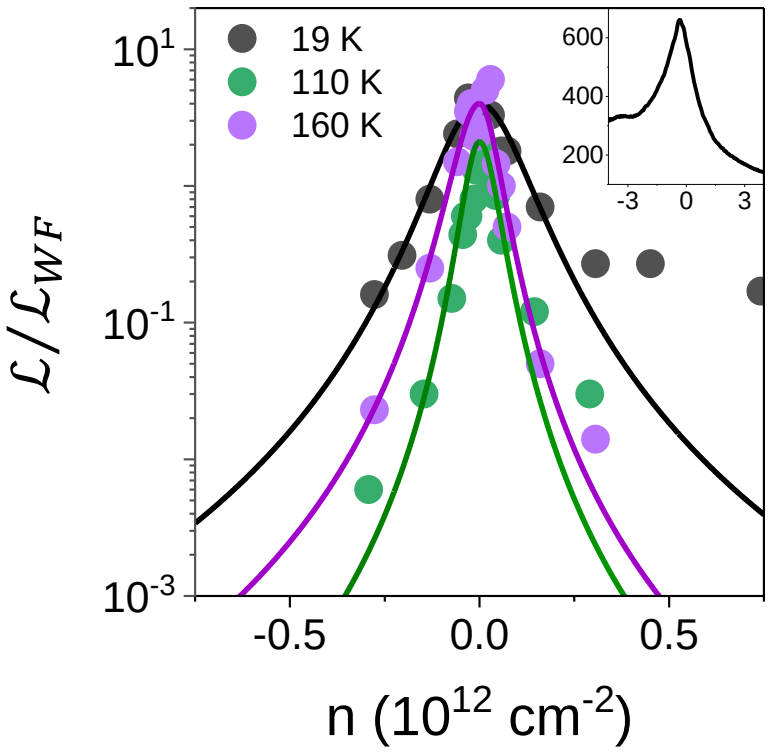

Extended Data Figure 4: **Carrier density- and temperature-dependence of the Lorentz number in D1S1:** Normalised Lorentz ratio ($\mathcal{L}/\mathcal{L}_{WF}$) for D1S1, as a function of n for three different T. The solid lines are theoretical fits for the experimental data, as per Eqn. 3. Inset shows the transfer characteristics of D1S1 at $T = 40$ K. The y-axis shows the electrical resistance in ohms while the x-axis shows the applied gate voltage V_g in volts. Further electrical characterisation of D1S1 indicating its intrinsic charge inhomogeneity and mobility are mentioned in Table I in Supplementary Information.

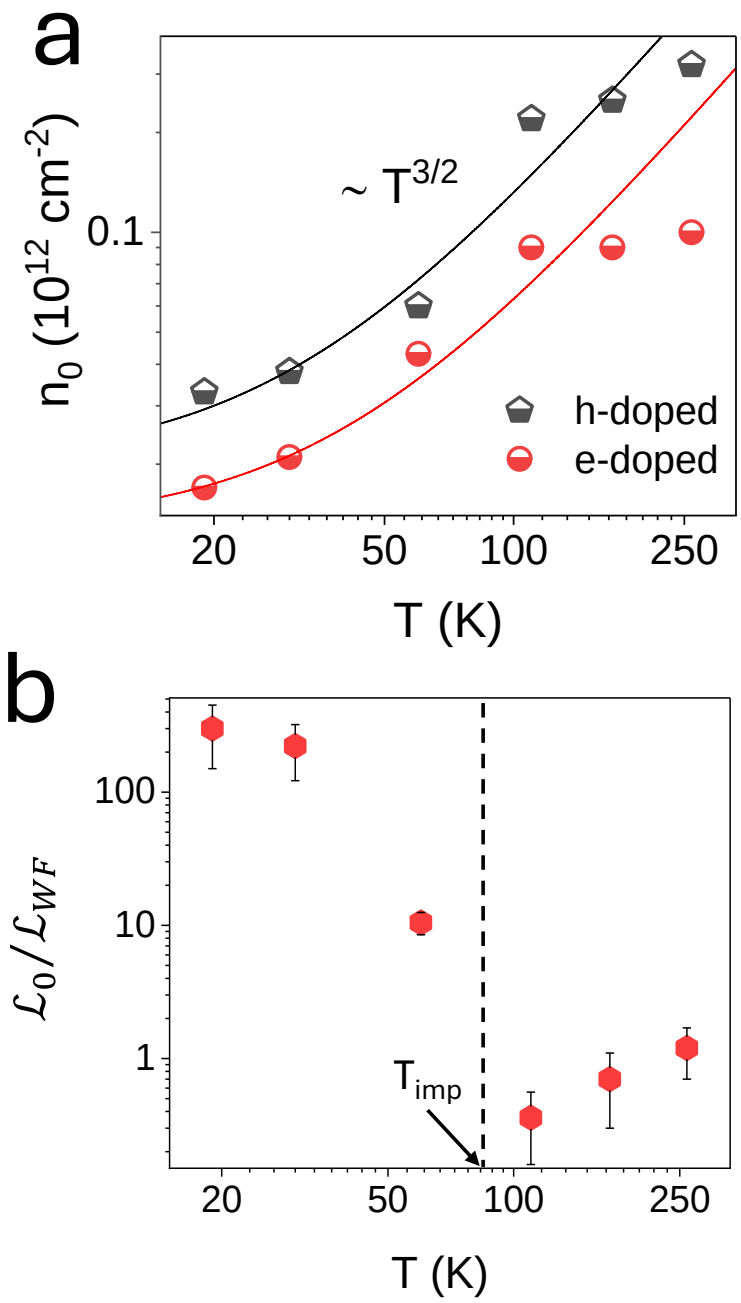

Extended Data Figure 5: **Characteristic scales of Lorentz number variation with density and temperature in D2S1:** (a) The characteristic density scale n_0 as a function of T, for the electron- and hole-doped ranges of D2S1. The solid lines show a $T^{3/2}$ fit of the experimental data points. (b) Normalised Lorentz ratio at the Dirac point ($\mathcal{L}_0/\mathcal{L}_{WF}$) of D2S1, as a function of T. The dashed line indicates the $T_{\rm imp}$ for D2S1.

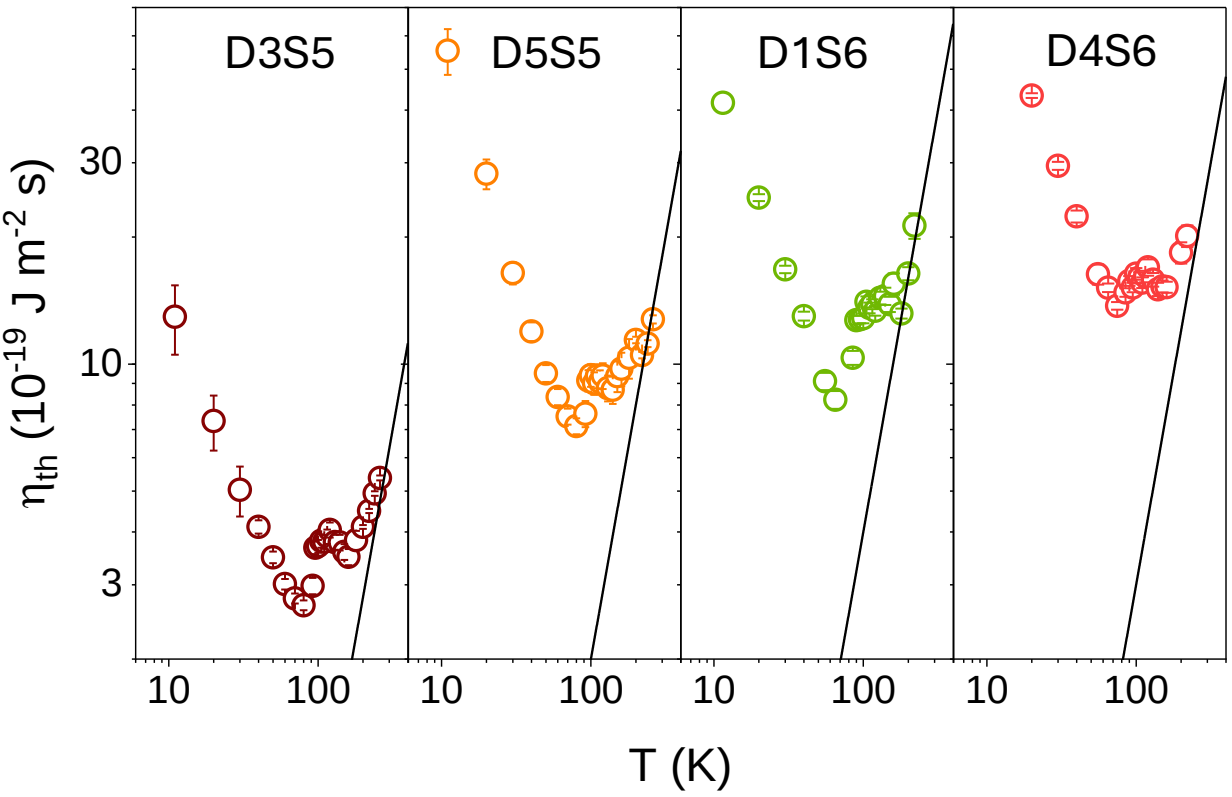

Extended Data Figure 6: **Non-monotonic temperature dependence of electron viscosity for additional devices:** $\eta_{\rm th}$ vs T for four devices D3S5, D5S5, D1S6 and D4S6. The non-monotonic trend is consistent across all the devices and approaches $\sim T^2$ for $T > T_{\rm imp}$. The black solid lines in each panel represent T^2 dependence.